

# New Class of Electrocatalysts Based on 2D Transition Metal Dichalcogenides in Ionic Liquid

*Leily Majidi, Poya Yasaei, Robert E. Warburton, Shadi Fuladi, John Cavin, Xuan Hu, Zahra Hemmat, Sung Beom Cho, Pedram Abbasi, Márton Vörös, Lei Cheng, Baharak Sayahpour, Igor L. Bolotin, Peter Zapol, Jeffrey Greeley, Robert F. Klie, Rohan Mishra, Fatemeh Khalili-Araghi, Larry A. Curtiss,\* and Amin Salehi-Khojin\**

The optimization of traditional electrocatalysts has reached a point where progress is impeded by fundamental physical factors including inherent scaling relations among thermokinetic characteristics of different elementary reaction steps, non-Nernstian behavior, and electronic structure of the catalyst. This indicates that the currently utilized classes of electrocatalysts may not be adequate for future needs. This study reports on synthesis and characterization of a new class of materials based on 2D transition metal dichalcogenides including sulfides, selenides, and tellurides of group V and VI transition metals that exhibit excellent catalytic performance for both oxygen reduction and evolution reactions in an aprotic medium with Li salts. The reaction rates are much higher for these materials than previously reported catalysts for these reactions. The reasons for the high activity are found to be the metal edges with adiabatic electron transfer capability and a cocatalyst effect involving an ionic-liquid electrolyte. These new materials are expected to have high activity for other core electrocatalytic reactions and open the way for advances in energy storage and catalysis.

Within a broad space of materials that have been explored for electrocatalytic applications, several 2D and quasi-2D structures have recently been reported to exhibit superior properties for the hydrogen evolution reaction and other core

electrochemical reactions.<sup>[1–11]</sup> In particular, molybdenum disulfide ( $\text{MoS}_2$ ) and a few members of transition metal dichalcogenides (TMDCs) in contact with ionic-liquid (IL) electrolyte have recently shown a great promise to overcome fundamental electronic and thermokinetic limitations for  $\text{CO}_2$  reduction reaction, as well as the oxygen reduction and evolution reactions (ORR/OER).<sup>[7–10]</sup> These studies have been conducted on a limited number of TMDCs, and the majority of other TMDCs with a wide range of electronic and potentially catalytic properties have not been investigated. In this study, we report synthesis and characterization of a wide range of TMDCs including sulfides, selenides, and tellurides of group V and VI transition metals and study their electrochemical performance in aprotic medium with Li salts. We employ a wide suite of characterization techniques, such as scanning transmission electron microscopy (STEM), energy dispersive spectroscopy (EDS), Raman spectroscopy, X-ray photoelectron spectroscopy (XPS), ultraviolet photoelectron spectroscopy (UPS), dynamic light scattering (DLS), and atomic force

L. Majidi, Dr. P. Yasaei, Z. Hemmat, P. Abbasi, B. Sayahpour,

Prof. A. Salehi-Khojin

Department of Mechanical and Industrial Engineering  
University of Illinois at Chicago

Chicago, IL 60607, USA

E-mail: salehikh@uic.edu

R. E. Warburton, Prof. J. Greeley

Davidson School of Chemical Engineering

Purdue University

West Lafayette, IN 47907, USA

S. Fuladi, X. Hu, Prof. R. F. Klie, Prof. F. Khalili-Araghi

Department of Physics

University of Illinois at Chicago

Chicago, IL 60607, USA

J. Cavin

Department of Physics

Washington University in St. Louis  
St. Louis, MO 63130, USA

Dr. S. B. Cho, Prof. R. Mishra

Department of Mechanical Engineering & Materials Science

Washington University in St. Louis

St. Louis, MO 63130, USA

Dr. M. Vörös, Dr. L. Cheng, Dr. P. Zapol, Dr. L. A. Curtiss

Materials Science Division

Argonne National Laboratory

Argonne, IL 60439, USA

E-mail: curtiss@anl.gov

Prof. I. L. Bolotin

Department of Chemistry

University of Illinois at Chicago

Chicago, IL 60607, USA

 The ORCID identification number(s) for the author(s) of this article can be found under <https://doi.org/10.1002/adma.201804453>.

DOI: 10.1002/adma.201804453

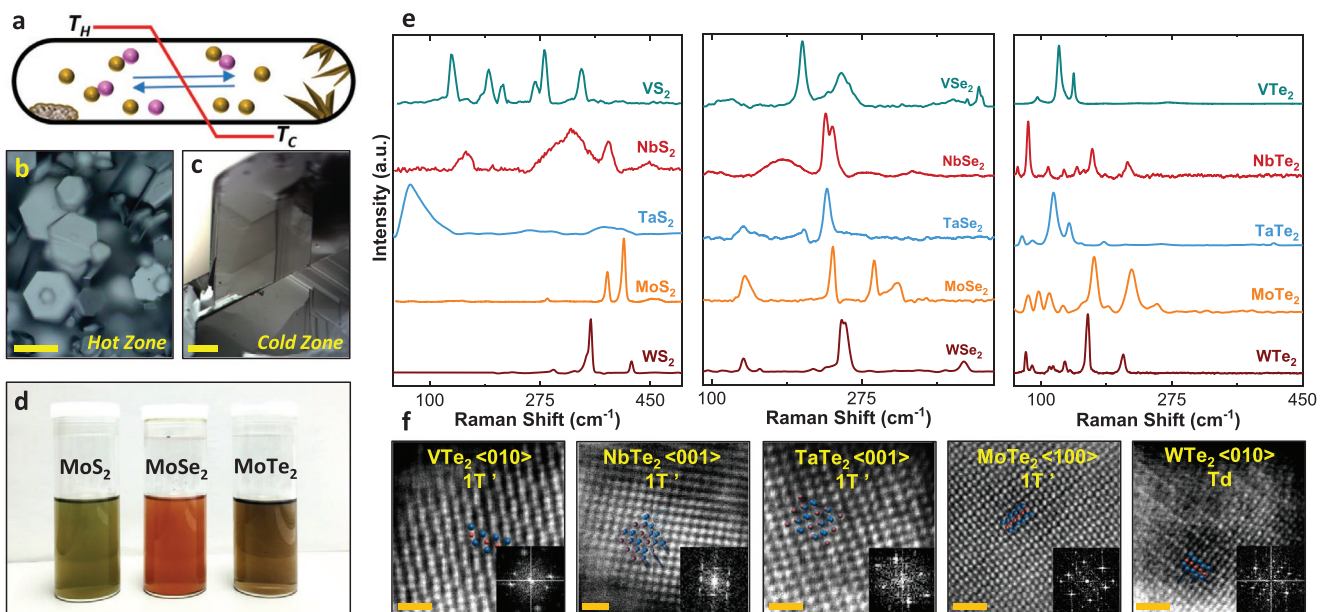


**Figure 1.** Summary of crystal synthesis and structural characterizations. a) Schematic of the crystal synthesis method including a tube furnace with hot and cold temperature zones ( $T_H$  and  $T_C$ ). b) Optical microscopy image of the powder crystals formed at the hot zone. Scale bar is 25  $\mu\text{m}$ . c) Optical microscopy image of the larger crystals formed at the cold zone through direct transport of the precursor vapors. Scale bar is 25  $\mu\text{m}$ . d) Photograph of the synthesized solutions of  $\text{MoS}_2$ ,  $\text{MoSe}_2$ , and  $\text{MoTe}_2$  through liquid-phase exfoliation in IPA followed by centrifugation and supernatant collection. e) Raman spectra of all the group V and VI TMDC crystals studied in this report. f) Atomic-resolution TEM images of the transition metal tellurides with different crystalline faces. Insets show the FFT patterns. Scale bar is 1 nm.

microscopy (AFM), as well as computational simulations, to elucidate structural, atomic, and electronic characteristics of the synthesized materials.

Bulk TMDCs were synthesized through a direct reaction of pure elements followed by a chemical vapor transport (CVT) process in an evacuated quartz ampule at high temperatures. The powders of the transition metals and chalcogens were mixed in desired stoichiometric ratios and loaded in quartz ampules. The ampules were then evacuated, sealed, and placed in a two-zone furnace for the crystal growth process. Details of the material synthesis are provided in the Experimental Section and Section S1 of the Supporting Information. Figure 1a shows the schematic of the crystal growth process. After the synthesis process, a powder of TMDC single-crystalline flakes is usually obtained (Figure 1b) in the hot zone of the ampule. In the cold zone, single-crystalline chunks of the TMDC are formed through a direct transport of vaporized precursors (Figure 1c). Optical images of the synthesized materials in both zones show sharp geometrical features, implying that the reaction products are highly crystalline.

To prepare TMDC nanoflakes suitable for electrochemical experiments, a liquid-phase exfoliation technique was used (see the Experimental Section), which results in uniform dispersions of atomically thin nanoflakes in the solvent. For ease of exfoliation, we used the powders obtained in the hot-zone of the growth ampule. The material obtained in the cold zone usually requires further processing, i.e., grinding, to facilitate the liquid exfoliation. Figure 1d shows a photograph of sample dispersions of  $\text{MoS}_2$ ,  $\text{MoSe}_2$ , and  $\text{MoTe}_2$  in isopropyl alcohol (IPA) after sonication, centrifugation, and supernatant collection. In all the samples, the color of the dispersion is primarily determined

by the chalcogen type with minor variations due to different transition metals.

Raman spectroscopy was used to verify the successful synthesis of TMDCs. Figure 1e shows the sample Raman spectra of all 15 synthesized TMDCs studied in this report, indicating distinct peaks associated with different vibrational modes of the TMDC crystals. For instance, the major representative Raman peaks of  $\text{WS}_2$  are observed at 296.6, 350.5, 355.6, and 420.2  $\text{cm}^{-1}$  where the first two peaks match  $2\text{LA}(\text{M}) - 2\text{E}_{2g}^2(\text{M})$  and  $2\text{LA}(\text{M})$ , respectively, and the third and fourth peaks represent  $\text{E}_{2g}^1$  and  $\text{A}_{1g}^{[12]}$ . Raman spectrum of  $\text{TaSe}_2$  indicates the main peaks at 137.6, 207.3, and 234.5  $\text{cm}^{-1}$  which correspond to  $\text{E}_{1g}$ ,  $\text{E}_{2g}^1$ , and  $\text{A}_{1g}$ , respectively.<sup>[13]</sup>  $\text{WTe}_2$  Raman peaks are also shown at 79.6( $\text{A}_1$ ), 88.3( $\text{A}_2$ ), 111.5( $\text{A}_2$ ), 115.9( $\text{A}_2$ ), 131.2( $\text{A}_1$ ), 138.9( $\text{A}_1$ ), 162.59( $\text{A}_1$ ), and 209.7( $\text{A}_1$ )  $\text{cm}^{-1}$ .<sup>[14-16]</sup>

Figure 1f shows atomic-resolution high angle annular dark field (HAADF) images of selected five materials with simulated crystal structures (inserted). We find  $\text{NbTe}_2$ ,  $\text{TaTe}_2$ ,  $\text{VT}_2$  samples are in their  $1\text{T}'$  phase ( $C2/m$ , monoclinic) from side and top views, while  $\text{MoTe}_2$  is in its  $1\text{T}'$  phase ( $P2_1/m$ , monoclinic), and  $\text{WTe}_2$  is in its  $\text{Td}$  phase ( $Pmn2_1$ , orthogonal) from side views. X-ray EDS was carried out to probe the chemical composition of the nanoflakes and to determine the presence of impurities (Figure S1, Supporting Information). XPS was also utilized to evaluate the chemical states of synthesized TMDCs. Section S3 in the Supporting Information presents the corresponding XPS spectra for all of the synthesized TMDCs.

The liquid exfoliated dispersions were characterized by DLS and AFM to determine the lateral size and thickness

distributions of the exfoliated materials (as a representative, see Figures S6 and S7 in the Supporting Information). DLS results indicate an average size of 140–240 nm for all the TMDCs dispersions. AFM height measurements obtained from 30–40 randomly selected exfoliated flakes show the thickness ranging from 2 to 44 nm with an average of about 15–24 nm.

UPS was used to measure work functions of the synthesized TMDCs. The work function has been shown previously to be a good descriptor for catalytic activity in metal catalysts.<sup>[17]</sup> Moreover, it was shown that for MoS<sub>2</sub>, MoSe<sub>2</sub>, WS<sub>2</sub>, and WSe<sub>2</sub> nanoflakes, the catalytic activity for CO<sub>2</sub> reduction increases with decreasing work function.<sup>[10]</sup> Figure 2a shows the comparison among the obtained work functions of the synthesized TMDCs through UPS experiments and their theoretical values calculated using density-functional theory (DFT) within the generalized gradient approximation of Perdew–Burke–Ernzerhof (PBE).<sup>[18]</sup> As shown in Figure 2a, the UPS-measured work function values for these materials range from 2.95 to 5.14 eV. The lowest measured work function values were recorded for WTe<sub>2</sub> (2.95 eV) and TaTe<sub>2</sub> (3.11 eV). Figure 2a also shows the DFT-calculated work functions of the TMDCs. The color gradient bars in Figure 2a highlight semiconducting materials and their predicted range of possible work functions. These ranges correspond to the energies between the valence band

maximum (VBM) and conduction band minimum (CBM). While the PBE exchange-correlation functional satisfactorily calculates the energy levels of the occupied states including the VBM, it underestimates the energy of the empty states, such as the CBM.<sup>[19]</sup> Hence, it leads to bandgaps in semiconductors that are smaller than the experimental value.<sup>[20–22]</sup> To avoid this issue for the four semiconducting TMDCs (MoS<sub>2</sub>, MoSe<sub>2</sub>, WS<sub>2</sub>, and WSe<sub>2</sub>), we have used the experimental value of the bandgap to determine the position of the CBM<sup>[23]</sup> from the calculated VBM. In general, we find that for each family of TMDCs corresponding to a particular transition metal, the work function decreases from ≈6 to 4.5 eV as the mass of the chalcogen atom increases. For a given chalcogen atom though, we find a less dramatic change in the work function on varying the transition metal atom. However, we find a discrepancy between the experimental and theoretical values for MoTe<sub>2</sub>, WTe<sub>2</sub>, and the TaX<sub>2</sub> compounds. Discrepancies in work functions can possibly be attributed to a small oxidation of the surface that was observed in STEM EDS experiments. Formation of a very thin oxide layer, for instance on tantalum, has been shown to reduce its work function.<sup>[24]</sup> Nevertheless, the calculated trends for all the compounds are in excellent agreement with the experiments.

To understand how the composition of a TMDC affects its work function and if there is any correlation with catalytic

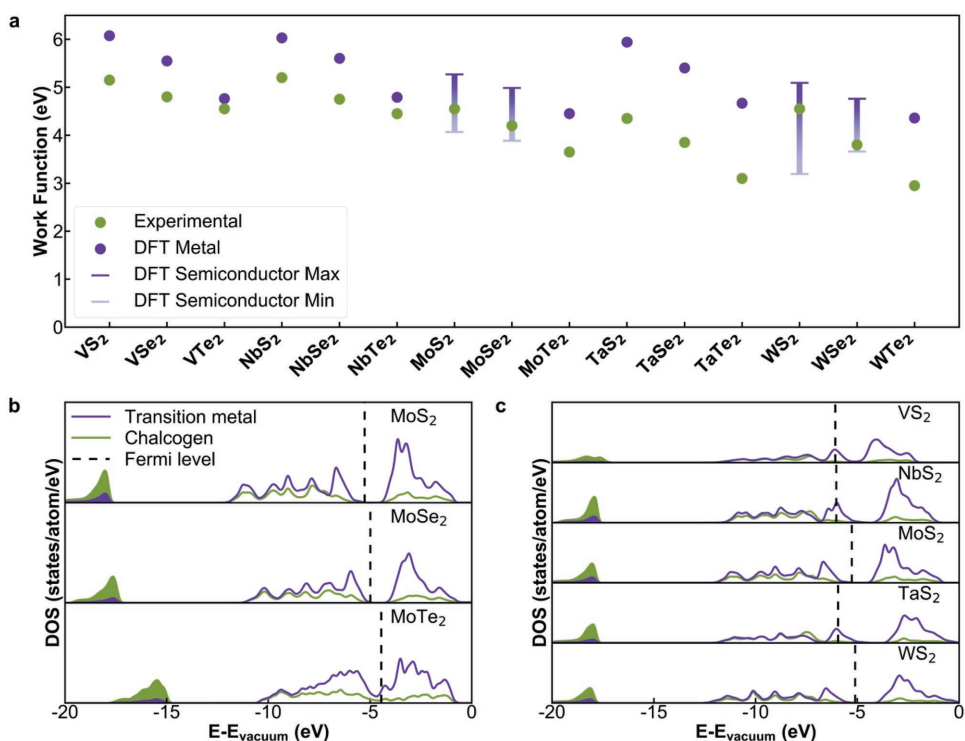


**Figure 2.** Experimental and theoretical work function and electronic structure of bulk MX<sub>2</sub>. a) The experimental and calculated work function of the 15 MX<sub>2</sub> TMDCs. The calculated work function of semiconducting materials is shown as a range representing a tunable region bounded by the valence band maximum and the conduction band minimum measured from the vacuum level. b) Comparison of atom-projected densities of states (DOS) for the transition metal and chalcogen atoms in MoS<sub>2</sub>, MoSe<sub>2</sub>, and MoTe<sub>2</sub>. Energies are relative to the vacuum level. On moving from S to Se to Te, both the semi-core states of the chalcogens (shaded) and the Fermi level shift to higher energies. This corresponds to a decrease in work function with increasing chalcogen mass. c) The atom-projected DOS for MoS<sub>2</sub>, WS<sub>2</sub>, VS<sub>2</sub>, NbS<sub>2</sub>, and TaS<sub>2</sub>. The sulfur semi-core states and the work function show little variation other than from one transition metal group to another.

activity, we have calculated the electronic structure of the TMDCs with selective variation of either the chalcogen or the transition metal. Figure 2b shows the atom-projected density of states (DOS) for MoS<sub>2</sub>, MoSe<sub>2</sub>, and MoTe<sub>2</sub>, where the energy is normalized with respect to the vacuum level. We observe that the semi-core s-states of the chalcogen atoms, indicated by the shaded region, shift to higher energies for heavier chalcogens. This trend is similar to the reduction in the work function for heavier chalcogens. Figure 2c, on the other hand, shows the atom-projected DOS of MoS<sub>2</sub>, VS<sub>2</sub>, NbS<sub>2</sub>, WS<sub>2</sub>, and TaS<sub>2</sub>. The semi-core s-states of the sulfur atoms do not show any appreciable variation. Likewise, we found that the work functions of the five compounds do not indicate much variation either, except when there is a transition from metal (Group V cation) to semiconductor (Group VI cation). We conclude that the work function reduction found in TMDCs with heavier chalcogens is directly correlated to the shift in the chalcogen semi-core states to higher energies.

After thorough characterization of the synthesized TMDCs, we examined their catalytic performances by carrying out electrochemical cyclic voltammetry (CV) experiments during ORR and OER. The dispersed TMDCs in IPA were used to prepare the cathodes through layer by layer coating on gas diffusion layer (GDL) substrates. The CV experiments were performed in a three electrode cell within a nonaqueous oxygen saturated electrolyte, containing 0.1 M lithium bis(trifluoromethanesulfonyl)imide salt and a hybrid electrolyte

of 1-ethyl-3-methylimidazolium tetrafluoroborate (EMIM-BF<sub>4</sub>) ionic liquid and dimethyl sulfoxide (DMSO) with a volumetric ratio of 1 to 3, respectively, which produces the maximum ORR and OER among other compositions.<sup>[7]</sup> In our three-electrode cell experiments, the synthesized TMDC catalysts on GDL were used as the working electrode and lithium chips (99.9%) as the auxiliary and reference electrodes. The CV experiments were performed in the potential range 2.0–4.2 V versus Li/Li<sup>+</sup> with a scan rate of 20 mV s<sup>-1</sup>.

**Figure 3a,b** demonstrates the obtained current density results for all the synthesized TMDC catalysts for ORR and OER at potentials of 2.0 and 4.2 V versus Li/Li<sup>+</sup>, respectively. This set of results depicts the catalytic activity of various TMDC chemistries toward ORR and OER, which had not been considered previously. There are four catalysts among the synthesized TMDCs which show remarkably high activity in both ORR and OER: MoS<sub>2</sub>, NbS<sub>2</sub>, VS<sub>2</sub>, and VSe<sub>2</sub>. Figure 3c,d compares the electrochemical performance for these bifunctional catalysts with the state of the art catalysts in aprotic media such as noble metals (i.e., Pt),<sup>[25–28]</sup> metal oxides (i.e., Mn<sub>3</sub>O<sub>4</sub>),<sup>[29,30]</sup> perovskite (i.e., La<sub>0.5</sub>Sc<sub>0.5</sub>CoO<sub>2.91</sub>),<sup>[31]</sup> and doped carbon nanomaterials (i.e., N-doped graphene).<sup>[32]</sup> The data were extracted from various references and the current density values were normalized based on the geometrical surface area of the cathode.<sup>[25,29–32]</sup> At a potential of 2.0 V, NbS<sub>2</sub> presents the best ORR performance with a high current density of

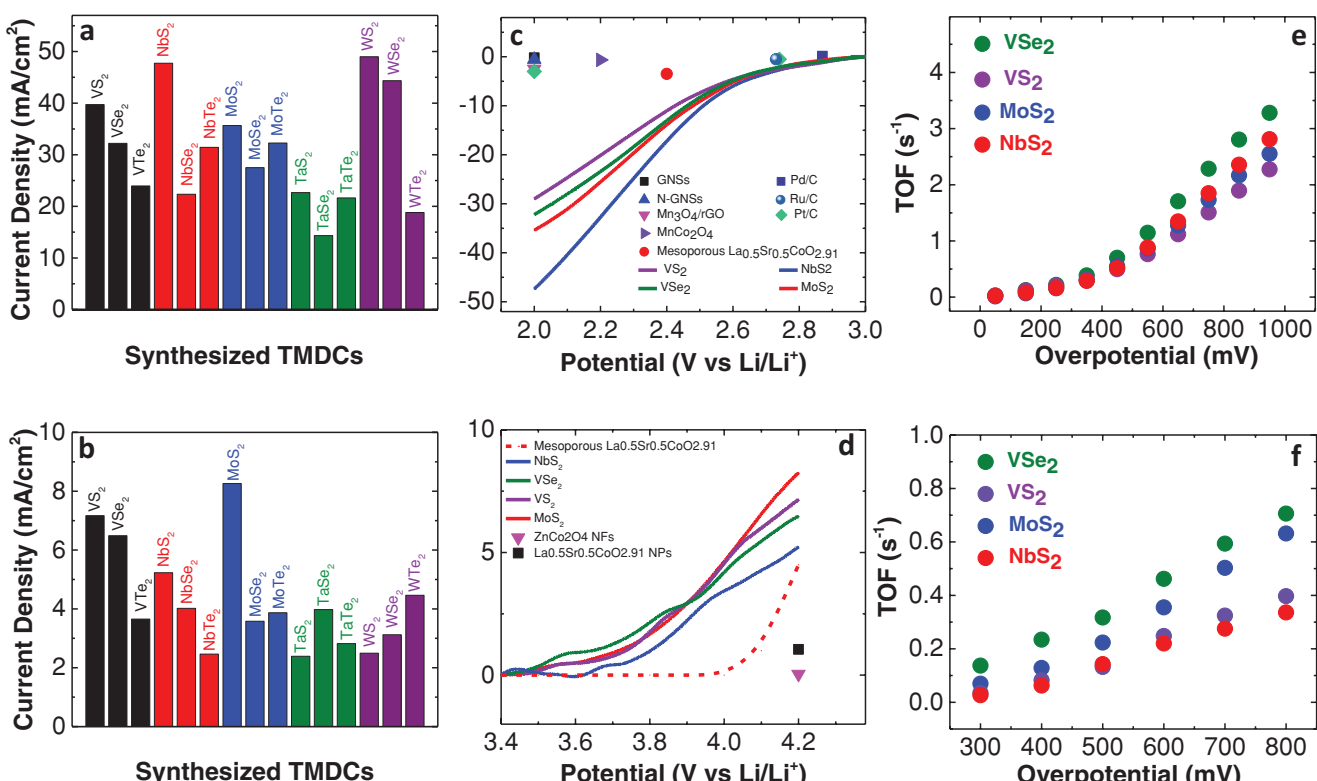


**Figure 3.** a,b) Performance comparison of synthesized TMDC catalysts in IL/DMSO mixture electrolyte for the oxygen reduction reaction (ORR) (a), and oxygen evolution reaction (OER) (b). c,d) ORR and OER of NbS<sub>2</sub>, MoS<sub>2</sub>, VS<sub>2</sub>, VSe<sub>2</sub> and other reported catalysts in aprotic media with Li salt.<sup>[25–27,29–32,45]</sup> The Y axis labels in (c) and (d) are the same as in (a) and (b). e,f) TOF of NbS<sub>2</sub>, MoS<sub>2</sub>, VS<sub>2</sub>, VSe<sub>2</sub> at different applied overpotentials during ORR and OER, respectively.

47.39 mA cm<sup>-2</sup>, which is  $\approx$ 15 times higher than that of Au, Pt, or commonly used oxides (i.e., Mn<sub>3</sub>O<sub>4</sub>)<sup>[29]</sup> at the same potential. NbS<sub>2</sub> also shows a current density of 5.22 mA cm<sup>-2</sup> at a potential of 4.2 V during OER, which is higher than the best reported catalyst (mesoporous La<sub>0.5</sub>Sr<sub>0.5</sub>CoO<sub>2.91</sub>)<sup>[31]</sup> in aprotic media for OER (current density of 4.5 mA cm<sup>-2</sup>, Figure 3d) obtained through rotating-disk electrode measurement in 1 M solution of LiPF<sub>6</sub> in ethylene carbon/dimethyl carbonate electrolyte. It is worth mentioning that the mesoporous La<sub>0.5</sub>Sr<sub>0.5</sub>CoO<sub>2.91</sub> catalyst shows an onset potential of  $\approx$ 4.0 V during OER, which is much higher than the TMDC materials reported in this work. This would increase the energy efficiency in TMDC compared to La<sub>0.5</sub>Sr<sub>0.5</sub>CoO<sub>2.91</sub> catalyst. VS<sub>2</sub> exhibits a current density of 39.72 and 7.17 mA cm<sup>-2</sup>, respectively, for the ORR and OER. VSe<sub>2</sub> and MoS<sub>2</sub> also have high current densities for both ORR and OER indicating a bifunctional behavior with remarkable performance for both ORR and OER in aprotic media. However, comparing Figure 2a with Figure 3a,b, we clearly see that lower work functions do not

correlate with higher ORR/OER activity, as was seen for CO<sub>2</sub> electroreduction.<sup>[10]</sup> Furthermore, in order to explore the intrinsic activity of our catalysts, a roughness factor technique<sup>[8–10,33,34]</sup> was used to measure the number of active sites and turn over frequency (TOF) values for MoS<sub>2</sub>, NbS<sub>2</sub>, VS<sub>2</sub>, and VSe<sub>2</sub>. TOF of these catalysts were calculated based on the current densities recorded at different overpotentials during ORR and OER. As depicted in Figure 3e, all of the four catalysts show similar TOF values during ORR where VSe<sub>2</sub> reaches the highest TOF of 3.28 s<sup>-1</sup> at the overpotential of 950 mV. Figure 3f shows the TOF values of these four catalysts during OER. At the overpotential of 800 mV, VSe<sub>2</sub> shows the highest TOF number of 0.7 s<sup>-1</sup>. (see Section S8 of the Supporting Information).

To better understand the mechanisms of ORR and OER on TMDC nanoflakes, we carried out more detailed computations using DFT and classical molecular dynamics (MD) simulations. In particular, MD simulations were used to determine distribution of electrolyte at the MoS<sub>2</sub>–solution interface. Figure 4a

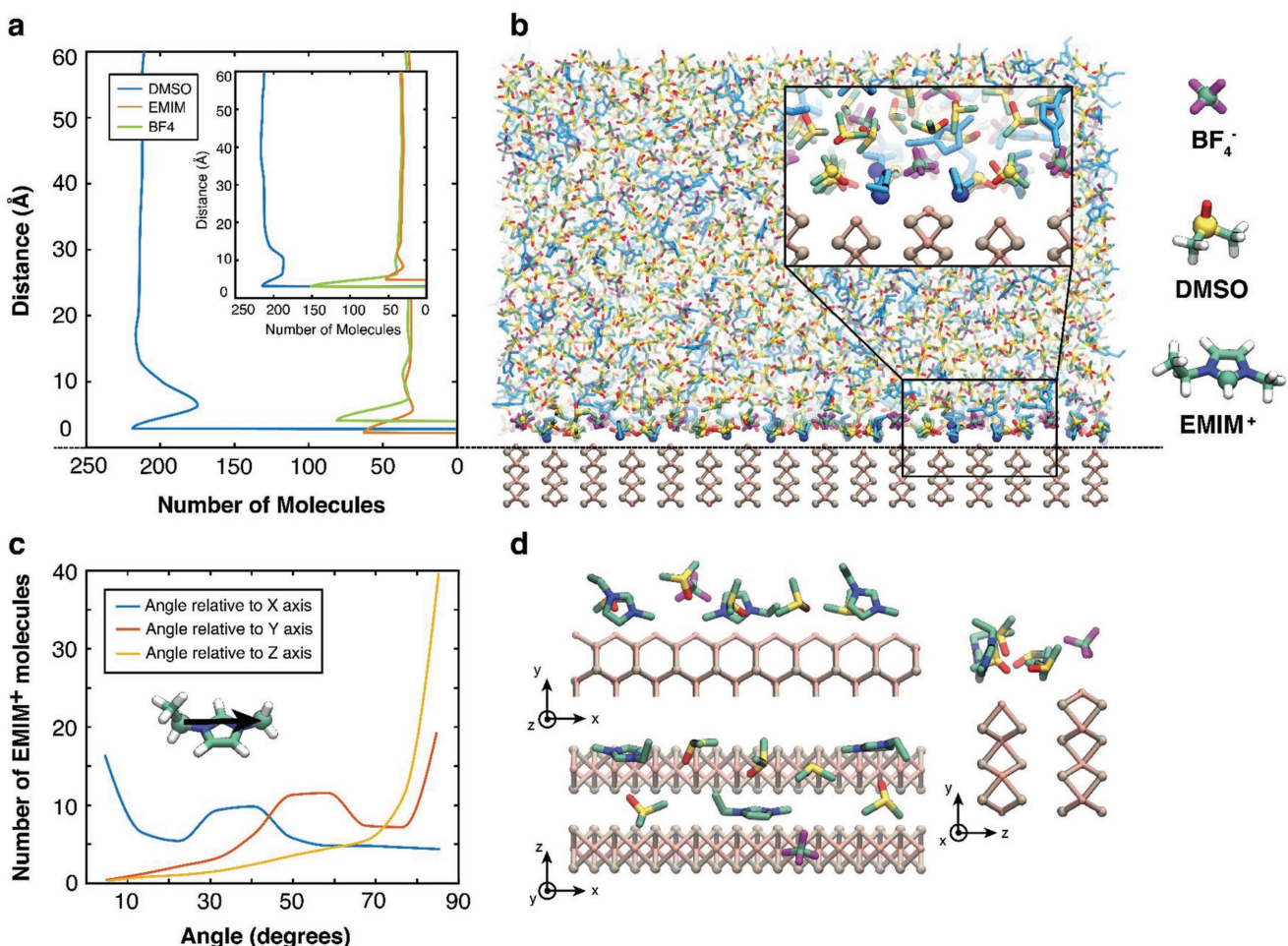


**Figure 4.** Molecular dynamics simulation results. a) Density profile of the EMIM<sup>+</sup>/BF<sub>4</sub><sup>-</sup>/DMSO mixture at its interface with metal-terminated sheets under an applied voltage bias obtained from molecular dynamics simulations. Inset represents the density profiles under equilibrium condition. The blue curve represents the density profile of sulfur atom of DMSO molecule, the green curve represents the density profile of boron atom of BF<sub>4</sub><sup>-</sup>, and the orange curve represents the density profile of the carbon atom of EMIM<sup>+</sup>, which is shown in (b). b) Snapshot of the simulation system showing 60 Å of the mixture near the metal-terminated surface, and molecular structure of the simulated ionic liquids and DMSO. c) The angle distribution of EMIM<sup>+</sup> cations with respect to the MoS<sub>2</sub> sheets obtained from molecular dynamics trajectories. Inset shows the defined vector along the length of EMIM<sup>+</sup> cations. d) Snapshots of the metal–mixture interface from different viewpoints showing the orientation of interacting molecules.

shows the density profile of EMIM<sup>+</sup>, BF<sub>4</sub><sup>-</sup>, and DMSO molecules across the simulation box normal to the MoS<sub>2</sub> surface. Under equilibrium conditions, mostly DMSO and BF<sub>4</sub><sup>-</sup> molecules are interacting with the MoS<sub>2</sub> surface, due to the positive charge density of the surface, while EMIM<sup>+</sup> cations are forming the dense wall a bit further away from the surface (inset of Figure 4a). Application of an electric field normal to the MoS<sub>2</sub> surface (as described in Section S9 of the Supporting Information) forces BF<sub>4</sub><sup>-</sup> anions away from the surface and makes it accessible to EMIM<sup>+</sup> molecules (Figure 4a,b). Figure 4c,d shows the orientation of EMIM<sup>+</sup> cations near the Mo terminated MoS<sub>2</sub> sheets. As shown in Figure 4c,d, the majority of EMIM<sup>+</sup> molecules lie parallel to the interface, align with MoS<sub>2</sub> sheets, and lie between two adjacent sheets. A fraction of EMIM<sup>+</sup> cations are positioned at a  $\approx 50^\circ$ – $60^\circ$  angle with respect to the surface, with the ring closer to the surface and the carbon tail further away and making a  $\approx 30^\circ$ – $40^\circ$  angle with each MoS<sub>2</sub> sheet.

Constrained density functional theory (CDFT) calculations were then carried out on MoS<sub>2</sub> and WS<sub>2</sub> to investigate the nature of the electron transfer in the ORR and OER mechanisms to obtain insight into the high electrocatalytic activity of these materials. The presence of diabatic electron transfer during ORR or OER would involve direct electron hopping, as opposed to electron transfer upon adsorption/desorption, between the catalyst and O<sub>2</sub> or Li<sub>2</sub>O<sub>2</sub>, i.e., adiabatic electron transfer. CDFT is used here because it allows for proper charge localization between groups of atoms corresponding to the donor ( $\mathcal{D}$ ) and acceptor ( $\mathcal{A}$ ) states during charge transfer. Further, this enables calculation of electronic couplings ( $H_{ab}$ ) between initial and final electronic states, in order to gain insights into the kinetics of electron transfer, i.e., through Marcus theory for diabatic charge transfer.<sup>[35]</sup>

The catalytically active sites of MoS<sub>2</sub> and WS<sub>2</sub> are typically at the edges,<sup>[36]</sup> which STEM experiments have determined to be metal-terminated for this particular synthesis process.<sup>[10]</sup> We applied a cluster model with periodic boundary conditions

(shown in Figure 5a), modified from the one used previously by Huang et al.<sup>[37]</sup> to expose a metal-terminated edge with adsorbed (EMIM<sup>+</sup> + e<sup>-</sup>) pairs, which bind strongly to the cathode.<sup>[8]</sup> The edges are passivated with 0.5 ML of the chalcogenide ion (sulfur in this case), with an additional sulfur ion positioned at the free corner (opposite side of cluster from adsorbed EMIM<sup>+</sup> ions and active metal site, Figure 5a). This ensures that unpaired electrons on the isolated metal site of the flake edge represent the highest occupied molecular orbital (HOMO) of the system. For ORR, we consider charge hopping from the flake to an O<sub>2</sub> molecule, leading to superoxide ion (O<sub>2</sub><sup>-</sup>) formation (Figure 5b). The subsequent reaction with Li<sup>+</sup> ions to form the Li<sub>2</sub>O<sub>2</sub> in the EMIM<sup>+</sup>/BF<sub>4</sub><sup>-</sup> solvent is facile, as shown previously.<sup>[8]</sup> OER, however, involves the oxidation of the O<sub>2</sub><sup>2-</sup> anions in Li<sub>2</sub>O<sub>2</sub>. As a model for the onset of OER, we introduce a hole onto the catalyst, corresponding to electron removal from the flake HOMO, which is calculated to be thermodynamically favorable under OER conditions (Figure S7, Supporting Information). We then consider the transfer of an electron from a neutral Li<sub>2</sub>O<sub>2</sub> monomer to fill the induced hole on the flake, such that the O<sub>2</sub> anion in Li<sub>2</sub>O<sub>2</sub> is oxidized from O<sub>2</sub><sup>2-</sup> (peroxide) to O<sub>2</sub><sup>-</sup> (superoxide), as shown in Figure 5c.

A summary of the Marcus rate parameters for ORR and OER is included in Table 1. The electronic couplings are exponential in distance between the donor and acceptor ( $r_{D-A}$ ) due to the exponential decay of wave functions as a function of separation. A regression of the CDFT-calculated couplings is used to fit  $H_{ab}$  to the form:  $H_{ab} = A \exp\left(-\frac{\alpha}{2} r_{D-A}\right)$ , where  $A$  is a pre-exponential factor and  $\alpha$  is the decay rate. In general, we found that the  $H_{ab}$  decays more slowly for ORR, in comparison to OER, by approximately a factor of two. The reorganization energies ( $\lambda$ ) for OER, largely due to relaxation of the O<sub>2</sub><sup>-</sup> anion in Li<sub>2</sub>O<sub>2</sub>, are considerably larger than for ORR. The consequence is that the lower  $\lambda$  for ORR, in combination with a more unfavorable driving force ( $\Delta G$ ) for charge transfer, makes the activation energy ( $E_{act}$ ) for this proposed diabatic charge hopping process prohibitively high. The O<sub>2</sub> binds to TMDC nanoflake edges very

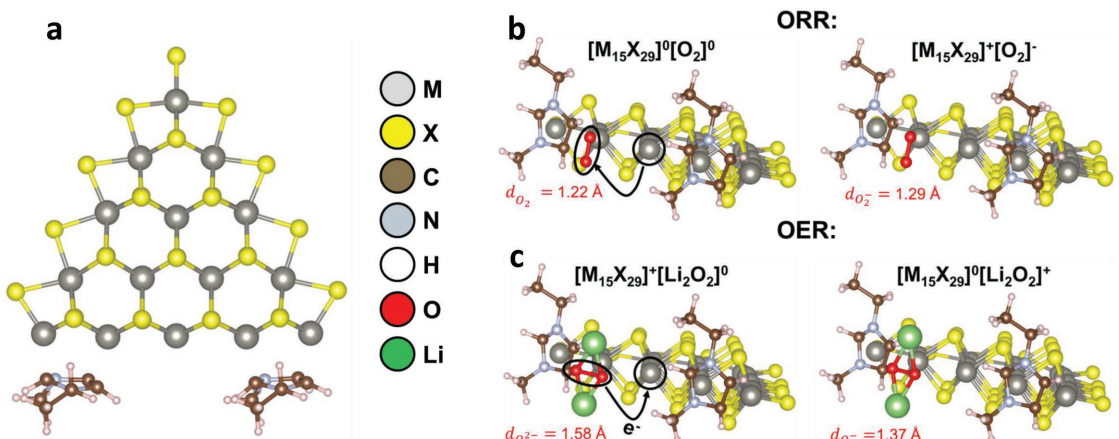


**Figure 5.** Molecular cluster models used for constrained density functional theory (CDFT) calculations. a)  $M_{15}X_{29}$  cluster with two (EMIM<sup>+</sup> + e<sup>-</sup>) pairs adsorbed on the metal-terminated edge, where M represents the metal cations and X represents the chalcogen anions. The isolated metal site between the EMIM<sup>+</sup> molecules represents the active site for electron transfer during oxygen reduction and evolution. b) Charge hopping from  $[M_{15}X_{29}]^0$  to  $[M_{15}X_{29}]^+$  to convert O<sub>2</sub> to O<sub>2</sub><sup>-</sup> (superoxide ion) during ORR. c) Charge hopping from Li<sub>2</sub>O<sub>2</sub> monomer to  $[M_{15}X_{29}]^0$  with a hole localized on the active site, converting the Li<sub>2</sub>O<sub>2</sub> (peroxide anion) to Li<sub>2</sub>O<sub>2</sub><sup>-</sup> (superoxide anion).

**Table 1.** Driving forces ( $\Delta G$ ), reorganization energies ( $\lambda$ ), activation energies ( $E_{act}$ ), and electronic coupling pre-exponential ( $A$ ) and decay rate ( $\alpha$ ) regression fit parameters for charge hopping ORR and OER mechanisms.

Transition		$\Delta G$ [eV]	$\lambda$ [eV]	$E_{act}$ [eV]	$A$ [eV]	$\alpha [\text{Å}^{-1}]$
ORR:	$[\text{Mo}_{15}\text{S}_{29}]^0[\text{O}_2]^0 \rightarrow [\text{Mo}_{15}\text{S}_{29}]^+[\text{O}_2]^-$	2.94	0.39	7.14	325	1.61
	$[\text{W}_{15}\text{S}_{29}]^0[\text{O}_2]^0 \rightarrow [\text{W}_{15}\text{S}_{29}]^+[\text{O}_2]^-$	2.85	0.44	6.14	92	1.35
OER:	$[\text{Mo}_{15}\text{S}_{29}]^0[\text{Li}_2\text{O}_2]^0 \rightarrow$ $[\text{Mo}_{15}\text{S}_{29}]^+[\text{Li}_2\text{O}_2]^+$	0.87	1.01	0.87	20 541	2.49
	$[\text{W}_{15}\text{S}_{29}]^0[\text{Li}_2\text{O}_2]^0 \rightarrow$ $[\text{W}_{15}\text{S}_{29}]^+[\text{Li}_2\text{O}_2]^+$	0.96	0.98	0.96	50 681	2.58

strongly,<sup>[8]</sup> however, whereupon it is likely to be reduced adiabatically due to the large ground state charge transfer associated with binding to the nanoflake edge. With a higher  $\lambda$  for OER, the  $E_{act}$  for diabatic charge transfer is reduced. Moreover, it is unlikely that  $\text{O}_2$  anions bound to  $\text{Li}^+$  ions will be stable at the catalyst edge, based on calculated binding energies and reduction potentials (see discussion in Section S11 of the Supporting Information). It is therefore reasonable that the OER may proceed via diabatic charge transfer from the  $\text{Li}_2\text{O}_2$  charge product, which may also help explain why OER rates are considerably lower than ORR rates for these materials. The adiabatic nature of the ORR can explain the high electrocatalytic activity for ORR.

In summary, we synthesized 15 members of TMDC family through CVT method and explored their potential for electrocatalysis applications such as ORR and OER. Various characterization techniques were employed to understand the electronic and structural properties of these materials. It was shown that most of the tested catalysts exhibit bifunctionality for ORR and OER, four members including  $\text{NbS}_2$ ,  $\text{MoS}_2$ ,  $\text{VS}_2$ , and  $\text{VSe}_2$  depicted excellent performances, exceeding those of the well-known catalysts in aprotic media for both of these reactions. These results show a great potential to seek highly efficient bifunctional catalysts among TMDCs which have been rarely studied for electrochemical reactions beyond hydrogen evolution.

## Experimental Section

**Crystal Growth:** A total of 1 g of precursor powders of transition metal and chalcogen with a 1:2 stoichiometric ratio were loaded in an evacuated and sealed quartz ampule. The ampule was then placed in a two-zone furnace and the temperature of the both zones was raised to 1080 °C in one day. The temperature of the empty part of the ampule (cold zone) was then gradually cooled down to 950 °C in four days, while the other end was maintained at 1080 °C. The system was then slowly cooled down to room temperature in one day.

**Synthesis of TMDC Nanoflakes:** TMDC nanoflakes were synthesized using a liquid exfoliation method by sonicating a solution containing a mixture of 300 mg of the TMDC powder dispersed in 60 mL IPA. The sonication was carried out for 30 h using a probe sonicator (Vibra Cell Sonics 130 W). The resultant dispersions were centrifuged for 60 min at 2000 rpm, and the supernatant was collected.

**Raman Spectroscopy:** The Raman spectra were obtained using a Horiba LabRAM HR Evolution confocal Raman microscope using a 532 nm laser wavelength and 50× objective with Horiba Andor detector.

**XPS:** A Thermo Scientific ESCALAB 250Xi instrument was used to obtain XPS results. All spectra were calibrated based on the C–C bond binding

energy at 284.8 eV. Thermo Avantage software was used to analyze and process each element's data.

**AFM:** A Bruker ICON Dimension was used to obtain the topography maps of drop-cast flakes which are analyzed to get the statistical flake thickness distributions. Exfoliated TMDC dispersions in IPA were drop-cast on silicon substrates. The substrates were carefully washed by acetone, IPA, and deionized water before experiment to remove the solvent residues.

**DLS Measurement:** Flake size measurements were carried out using the Malvern Zetasizer Nano ZSP system at 25 °C. The instrument includes a 10 mW semiconductor laser with 633 nm emissions. TMDC NFs dispersed in IPA were used

for the measurements.

**Transmission Electron Microscopy (TEM):** Aberration corrected JEOL ARM200CF (S) TEM microscope, equipped with a cold field emission gun allowing for 0.8 Å spatial resolution and an Oxford X-max 100TLE windowless X-ray detector, was utilized for atomic resolution imaging and EDS. HAADF detector with 90 mrad inner-detector angle and 22 mrad probe convergence angle was utilized to obtain Z contrast images.

**UPS:** The UPS experiment was performed with He I UV source and in ultrahigh vacuum with the pressure of  $8.0 \times 10^{-10}$  mbar. A silver metal was used to first calibrate the analyzer based on the metal Fermi edge, and a bias of -10 V was applied in all cases to distinguish the sample energy cut-off from the cut-off of the spectrometer. Thermo Avantage software was used to analyze and process each synthesized material's data.

**Electrochemical Experiments:** The catalytic activity of the synthesized TMDCs nanoflakes for ORR and OER were studied by electrochemical experiments in a standard three-electrode cell (Section S7 of the Supporting Information). To prepare the cathode electrode, 100 mg of catalyst was coated onto a 1 cm<sup>2</sup> carbon paper (TGP-H-030, purchased from FuelCellsEtc) as a gas diffusion layer and dried overnight in an argon filled glove box.

**Constrained DFT Calculations:** To assess charge hopping rates ( $k_{CT}$ ) between nanoflakes and reaction intermediates, CDFT calculations were performed,<sup>[38,39]</sup> as implemented<sup>[40,41]</sup> in the QUANTUM-ESPRESSO code.<sup>[42]</sup> The generalized gradient approximation of PBE as the exchange-correlation functional was used.<sup>[18]</sup> The core states were treated using the optimized norm-conserving Vanderbilt pseudopotentials with a wave function kinetic energy cutoff of 80 Ry (1088 eV).<sup>[43,44]</sup>

## Supporting Information

Supporting Information is available from the Wiley online library or the author.

## Acknowledgements

The work of A.S.-K., R.F.K., L.M., P.Y., Z.H., X.H., P.A., and B.S. was supported by the National Science Foundation DMREF Grant 1729420. X.H. and R.F.K. also acknowledge funding from the National Science Foundation (Grant No. DMR-0959470, DMR-1626065) for the acquisition of the UIC JEOL JEMARM200CF with the Gatan Quantum GIF EELS spectrometer. The work at Washington University (J.C., S.B.C., and R.M.) was supported through NSF DMREF Grant 1729787. This work used the computational resources of the Extreme Science and Engineering Discovery Environment (XSEDE), which was supported by National Science Foundation grant number ACI-1053575, Bebop, a high-performance computing cluster operated by the Laboratory Computing Resource Center at Argonne National Laboratory, and the National Energy Research Scientific Computing Center (NERSC). The work of F.K.-A. and S.F. was supported by the National Science Foundation (Grant No. EFRI-1542864) and University of Illinois

at Chicago start-up fund. The authors acknowledge the Advanced Cyberinfrastructure for Education and Research (ACER) group at The University of Illinois at Chicago for providing HPC resources that have contributed to the research results reported within this paper. URL: <https://acer.uic.edu>.

Work by P.Z. and L.A.C. was supported by the US Department of Energy, BES Materials Sciences under Contract DEAC02-06CH11357 with UChicago Argonne, LLC, operator of Argonne National Laboratory. Work by L.C. was supported by the Joint Center for Energy Storage Research (JCESR), an Energy Innovation Hub funded by the U.S. Department of Energy, Office of Science, Basic Energy Sciences. The work of J.G. was supported through a Department of Energy award through the Office of Science, Office of Basic Energy Sciences, Chemical, Biological, and Geosciences Division, under award number DE-SC0010379. R.E.W. acknowledges support from the U.S. Department of Energy, Office of Science, Office of Workforce Development for Teachers and Scientists, Office of Science Graduate Student Research (SCGSR) Program. The SCGSR program is administered by the Oak Ridge Institute for Science and Education (ORISE) for the DOE. ORISE is managed by ORAU under contract number DE-SC0014664. M.V. was supported by Laboratory Directed Research and Development (LDRD) funding from Argonne National Laboratory, provided by the Director, Office of Science, of the U.S. Department of Energy under Contract No. DE-AC02-06CH11357. The authors thank Dr. Xinqi Chen at Atomic and Nanoscale Characterization Experimental Center (NUANCE) in Northwestern University for helpful guidance and discussions.

L.M. synthesized the TMDCs and their nanoflakes, and carried out the electrochemical experiments. L.M. and Z.H. performed UPS. I.L.B. supervised UPS analyses. Z.H. and B.S. performed Raman experiments. P.A., Z.H., P.Y., and L.M. carried out XPS and obtained AFM and DLS results. A.S.-K. supervised the electrochemical and characterization experiments. S.F. and F.K.-A. performed classical molecular dynamics simulations. J.C., S.B.C., and R.M. carried out computational work function measurements. R.E.W., L.C., P.Z., M.V., J.G., and L.A.C. carried out the computational studies (CDFT) of TMDC/IL systems. X.H. and R.F.K. performed STEM and EELS experiments. All of the authors contributed to the manuscript before submission.

## Conflict of Interest

The authors declare no conflict of interest.

## Keywords

electrocatalysis, ionic liquids, oxygen evolution reaction, oxygen reduction reaction, transition metal dichalcogenides

Received: July 12, 2018

Revised: October 19, 2018

Published online: November 30, 2018

- [1] M. Chhowalla, H. S. Shin, G. Eda, L.-J. Li, K. P. Loh, H. Zhang, *Nat. Chem.* **2013**, *5*, 263.
- [2] D. Voiry, J. Yang, M. Chhowalla, *Adv. Mater.* **2016**, *28*, 6197.
- [3] S. Manzeli, D. Ovchinnikov, D. Pasquier, O. V. Yazyev, A. Kis, *Nat. Rev. Mater.* **2017**, *2*, 17033.
- [4] Y. Qu, H. Pan, C. T. Kwok, *Sci. Rep.* **2016**, *6*, 1.
- [5] J. Yang, H. S. Shin, *J. Mater. Chem. A* **2014**, *2*, 5979.
- [6] L. Yang, P. Liu, J. Li, B. Xiang, *Catalysts* **2017**, *7*, 285.
- [7] M. Asadi, B. Sayahpour, P. Abbasi, A. T. Ngo, K. Karis, J. R. Jokisaari, C. Liu, B. Narayanan, M. Gerard, P. Yasaei, X. Hu, A. Mukherjee,

- K. C. Lau, R. S. Assary, F. Khalili-Araghi, R. F. Klie, L. A. Curtiss, A. Salehi-Khojin, *Nature* **2018**, *555*, 502.
- [8] M. Asadi, B. Kumar, C. Liu, P. Phillips, P. Yasaei, A. Behranginia, P. Zapol, R. F. Klie, L. A. Curtiss, A. Salehi-Khojin, *ACS Nano* **2016**, *10*, 2167.
- [9] P. Abbasi, M. Asadi, C. Liu, S. Sharifi-Asl, B. Sayahpour, A. Behranginia, P. Zapol, R. Shahbazian-Yassar, L. A. Curtiss, A. Salehi-Khojin, *ACS Nano* **2017**, *11*, 453.
- [10] M. Asadi, K. Kim, C. Liu, A. V. Addepalli, P. Abbasi, P. Yasaei, P. Phillips, A. Behranginia, J. M. Cerrato, R. Haasch, P. Zapol, B. Kumar, R. F. Klie, J. Abiade, L. A. Curtiss, A. Salehi-Khojin, *Science* **2016**, *353*, 467.
- [11] W. Choi, N. Choudhary, G. H. Han, J. Park, D. Akinwande, Y. H. Lee, *Mater. Today* **2017**, *20*, 116.
- [12] A. Berkdemir, H. R. Gutiérrez, A. R. Botello-Méndez, N. Perea-López, A. L. Elías, C. I. Chia, B. Wang, V. H. Crespi, F. López-Urías, J. C. Charlier, H. Terrones, M. Terrones, *Sci. Rep.* **2013**, *3*, 1.
- [13] J. A. Yan, M. A. Dela Cruz, B. Cook, K. Varga, *Sci. Rep.* **2015**, *5*, 1.
- [14] W. D. Kong, S. F. Wu, P. Richard, C. S. Lian, J. T. Wang, C. L. Yang, Y. G. Shi, H. Ding, *Appl. Phys. Lett.* **2015**, *106*, 081906.
- [15] Y. Cao, N. Sheremeteva, L. Liang, H. Yuan, T. Zhong, V. Meunier, M. Pan, *2D Mater.* **2017**, *4*, 035024.
- [16] Y. C. Jiang, J. Gao, L. Wang, *Sci. Rep.* **2016**, *6*, 1.
- [17] C. G. Vayenas, S. Bebelis, S. Ladas, *Nature* **1990**, *343*, 625.
- [18] J. P. Perdew, K. Burke, M. Ernzerhof, *Phys. Rev. Lett.* **1996**, *77*, 3865.
- [19] J. Paier, M. Marsman, K. Hummer, G. Kresse, I. C. Gerber, J. G. Angyán, *J. Chem. Phys.* **2006**, *124*, 154709.
- [20] P. Mori-Sánchez, A. J. Cohen, W. Yang, *Phys. Rev. Lett.* **2008**, *100*, 1.
- [21] L. J. Sham, M. Schäfer, *Phys. Rev. Lett.* **1983**, *51*, 1888.
- [22] J. P. Perdew, M. Levy, *Phys. Rev. Lett.* **1983**, *51*, 1884.
- [23] Q. H. Wang, K. Kalantar-Zadeh, A. Kis, J. N. Coleman, M. S. Strano, *Nat. Nanotechnol.* **2012**, *7*, 699.
- [24] D. L. Fehrs, R. E. Stickney, *Surf. Sci.* **1967**, *8*, 267.
- [25] Y.-C. Lu, H. A. Gasteiger, Y. Shao-Horn, *Electrochem. Solid-State Lett.* **2011**, *14*, A70.
- [26] Y. C. Lu, H. A. Gasteiger, Y. Shao-Horn, *J. Am. Chem. Soc.* **2011**, *133*, 19048.
- [27] Y.-C. Lu, H. A. Gasteiger, E. Crumlin, R. McGuire, Y. Shao-Horn, *J. Electrochem. Soc.* **2010**, *157*, A1016.
- [28] C. J. Allen, J. Hwang, R. Kautz, S. Mukerjee, E. J. Plichta, M. A. Hendrickson, K. M. Abraham, *J. Phys. Chem. C* **2012**, *116*, 20755.
- [29] Q. Li, P. Xu, B. Zhang, H. Tsai, J. Wang, H.-L. Wang, G. Wu, *Chem. Commun.* **2013**, *49*, 10838.
- [30] S. Ma, L. Sun, L. Cong, X. Gao, C. Yao, X. Guo, L. Tai, P. Mei, Y. Zeng, H. Xie, R. Wang, *J. Phys. Chem. C* **2013**, *117*, 25890.
- [31] Y. Zhao, L. Xu, L. Mai, C. Han, Q. An, X. Xu, X. Liu, Q. Zhang, *Proc. Natl. Acad. Sci. USA* **2012**, *109*, 19569.
- [32] Y. Li, J. Wang, X. Li, D. Geng, M. N. Banis, R. Li, X. Sun, *Electrochem. Commun.* **2012**, *18*, 12.
- [33] J. D. Benck, Z. Chen, L. Y. Kuritzky, A. J. Forman, T. F. Jaramillo, *ACS Catal.* **2012**, *2*, 1916.
- [34] J. Kibsgaard, Z. Chen, B. N. Reinecke, T. F. Jaramillo, *Nat. Mater.* **2012**, *11*, 963.
- [35] R. A. Marcus, *Rev. Mod. Phys.* **1993**, *65*, 599.
- [36] T. F. Jaramillo, K. P. Jørgensen, J. Bonde, J. H. Nielsen, S. Horch, I. Chorkendorff, *Science* **2007**, *317*, 100.
- [37] Y. Huang, R. J. Nielsen, W. A. Goddard, M. P. Soriaga, *J. Am. Chem. Soc.* **2015**, *137*, 6692.
- [38] B. Kaduk, T. Kowalczyk, T. Van Voorhis, *Chem. Rev.* **2012**, *112*, 321.
- [39] Q. Wu, T. Van Voorhis, *Phys. Rev. A - At. Mol. Opt. Phys.* **2005**, *72*, 7.
- [40] M. Vörös, N. P. Brawand, G. Galli, *Chem. Mater.* **2017**, *29*, 2485.
- [41] M. B. Goldey, N. P. Brawand, M. Vörös, G. Galli, *J. Chem. Theory Comput.* **2017**, *13*, 2581.

- [42] P. Giannozzi, S. Baroni, N. Bonini, M. Calandra, R. Car, C. Cavazzoni, D. Ceresoli, G. L. Chiarotti, M. Cococcioni, I. Dabo, A. D. Corso, S. de Gironcoli, S. Fabris, G. Fratesi, R. Gebauer, U. Gerstmann, C. Gougoussis, A. Kokalj, M. Lazzeri, L. Martin-Samos, N. Marzari, F. Mauri, R. Mazzarello, S. Paolini, A. Pasquarello, L. Paulatto, C. Sbraccia, S. Scandolo, G. Sclauzero, A. P. Seitsonen, A. Smogunov, P. Umari, R. M. Wentzcovitch, *J. Phys.: Condens. Matter* **2009**, *21*, 395502.
- [43] D. R. Hamann, *Phys. Rev. B* **2013**, *88*, 085117.
- [44] M. Schlipf, F. Gygi, *Comput. Phys. Commun.* **2015**, *196*, 36.
- [45] T.-F. Hung, S. G. Mohamed, C.-C. Shen, Y.-Q. Tsai, W.-S. Chang, R.-S. Liu, *Nanoscale* **2013**, *5*, 12115.